Check for updates

NANO · MICRO small
www.small-journal.com

Highly Sensitive Soft Pressure Sensors for Wearable Applications Based on Composite Films with Curved 3D Carbon Nanotube Structures

*Young Jung, Jimin Gu, Jinwook Yeo, Wookjin Lee, Hyeonseok Han, Jungrak Choi, Ji-Hwan Ha, Junseong Ahn, Hanchul Cho, Seunghwa Ryu, and Inkyu Park**

Soft pressure sensors based on 3D microstructures exhibit high sensitivity in the low-pressure range, which is crucial for various wearable and soft touch applications. However, it is still a challenge to manufacture soft pressure sensors with sufficient sensitivity under small mechanical stimuli for wearable applications. This work presents a novel strategy for extremely sensitive pressure sensors based on the composite film with local changes in curved 3D carbon nanotube (CNT) structure via expandable microspheres. The sensitivity is significantly enhanced by the synergetic effects of heterogeneous contact of the microdome structure and changes of percolation network within the curved 3D CNT structure. The finite-element method simulation is used to comprehend the relationships between the sensitivity and mechanical/electrical behavior of microdome structure under the applied pressure. The sensor shows an excellent sensitivity (571.64 kPa^{-1}) with fast response time (85 ms), great repeatability, and long-term stability. Using the developed sensor, a wireless wearable health monitoring system to avoid carpel tunnel syndrome is built, and a multi-array pressure sensor for realizing a variety of movements in real-time is demonstrated.

1. Introduction

Recently, soft pressure sensors have attracted significant interest for their various potential applications, such as wearable devices,[1] personal health monitoring,[2,3] human–motion interfaces,[4] and soft touch for entertainment systems.[5] For advanced applications such as healthcare and soft touch (0–10 kPa), the development of pressure sensors with high sensitivity (>1 kPa^{-1}) in the low-pressure range is essentially required. The mechanisms for detecting pressure can be divided into piezoresistive,[6–8] piezo-capacitive,[9–12] piezoelectric,[13] and piezo-transmittance[14] types. Soft pressure sensors based on piezoresistive type convert external pressure into a change in electrical resistance by varying the contact area between sensor's active layer and electrode. They have been widely used owing to their many advantages such as high sensitivity in the low-pressure range, easy operation, low fabrication cost, and simple structure.

To enhance the sensing performance of a piezoresistive-type pressure sensor, many researchers have utilized advanced materials, specifically soft, compressible, and deformable elastomer in recent time. However, due to the intrinsic material properties of the soft elastomers (e.g., viscoelasticity), pressure sensors based on them are still limited by insensitivity in the low-pressure range, hysteresis, and long response time. An efficient route for manufacturing soft pressure sensors with high sensitivity in the low-pressure range is to utilize 3D microstructures, such as pyramids,[10,15] domes,[6,16–18] and wrinkles.[19] These 3D microstructures cause a large local strain when pressure is applied, which greatly improves sensitivity and allows even small pressures to be detected. Additionally, using 3D microstructures helps to minimize the viscoelastic effects of elastomers, resulting in faster response, excellent limit of detection, and minimized hysteresis. Utilizing these 3D microstructures is being actively used to fabricate a variety of sensitive soft pressure sensors for many potential applications.

Soft pressure sensors have been proposed with the use of 3D microstructures, which are fabricated by a variety of methods. For example, Zhang et al. suggested sensitive pressure sensor based on interlocked microdome structure generated by colloid self-assembly and transfer.[18] The fabricated sensor exhibited a high sensitivity of ≈15 kPa^{-1} under 100 Pa and short response time (<100 ms) by optimizing the size of polystyrene microspheres. Yang et al. also proposed flexible pressure sensor based on interlocked bio-inspired microstructure deposited with thin

Y. Jung, J. Gu, J. Yeo, H. Han, J. Choi, J.-H. Ha, J. Ahn, S. Ryu, I. Park
Department of Mechanical Engineering
Korean Advanced Institute of Science and Technology (KAIST)
Daejeon 34141, Republic of Korea
E-mail: inkyu@kaist.ac.kr
W. Lee
School of Materials Science and Engineering
Pusan National University
Busan 46241, Republic of Korea
H. Cho
Precision Mechanical Process and Control R&D Group
Korea Institute of Industrial Technology (KITECH)
Busan 46938, Republic of Korea
The ORCID identification number(s) for the author(s) of this article can be found under https://doi.org/10.1002/smll.202303981

DOI: 10.1002/smll.202303981

 © 2023 Wiley-VCH GmbH

metal layer.[20] The designed sensor showed a high sensitivity of 53 kPa^{-1} and short response time of 38 ms, enabling the detection of a subtle pressure of weak air flow. The sensitivity based on piezoresistive type depends on the contact area between microstructure and electrode or other microstructure. For this reason, most of the proposed research focuses on the manufacturing strategy of the new type of 3D microstructures that are easily compressed and deformed.[16–18,20] However, despite its importance, conductive layers for the piezoresistive-type pressure sensors have not been well investigated. Therefore, a novel approach for changing the electrical property of the conductive layer under applied pressure and well-designed 3D microstructures is required to develop a new type of highly sensitive soft pressure sensor.

In this study, we propose a new strategy for highly sensitive soft pressure sensors based on a carbon nanotube (CNT)-elastomer composite film with local changes in curved 3D CNT structure (3DCS) via expansion of thermally expandable microspheres (TEMs). The active layer of the soft pressure sensor is made of flat 2D CNT structure and TEMs layer that are simultaneously embedded into the soft elastomer matrix. The expansion of TEMs by simple thermal treatment generates large local strains on the surface and changes CNTs structure embedded into the soft elastomer matrix from a flat 2D to a curved 3D geometry. The soft pressure sensor based on 3DCS has dramatically enhanced the sensitivity as a result of the synergetic effects of i) heterogeneous contact change of the irregular microdome structures and ii) contact pair change of percolation network within the 3D CNT structure due to the deformation of the microdome structure under the applied pressure. Furthermore, numerical simulations are employed to understand the relationships between the sensitivity and mechanical/electrical behavior (i.e., compressive behavior of microdome structure and change in curved 3D CNT structure) under the applied pressure. The proposed soft pressure sensor shows excellent sensing performance, including fast response, high repeatability, and long-term stability. To demonstrate the practical applications in wearable devices, wearable healthcare sensor was suggested to monitor the wrist pressure during daily mouse usage to prevent carpel tunnel syndrome. Finally, we verified that multi-array pressure sensor could realize a variety of real-time functions such as spatial pressure mapping.

2. Results and Discussion

2.1. Concept and Fabrication Process of 3DCS

To generate a large local strain and change the CNT network in the soft elastomer matrix, we use TEMs. The TEMs are commonly used as packaging, fillers, and blowing agents because of their expandability, scalability, and high mechanical stability. The TEMs consist of thermoplastic resins (acrylonitrile [AN] copolymers) at the outer shell and liquid hydrocarbon (isopentane) at the inside core.[21] When TEM is exposed at a specific temperature, the gasified hydrocarbon at the inside core permeates through the thin outer shell, eventually leaving no hydrocarbon gas inside the TEM. They expand by four to seven times of their original diameter as illustrated in **Figure 1**a. After complete expansion, TEM maintains its shape at room temperature due to plastic deformation of the outer shell. Figure 1b shows an overview of local changes in percolations and contact pairs between CNTs using TEMs expansion. Without TEMs expansion, the CNTs are densely embedded into the soft elastomer matrix and form many contact pairs as a flat 2D network. After heating, TEMs are expanded inside the soft elastomer matrix, generating large local strain, which changes the CNTs structure from a flat 2D to curved 3D geometry, leading to a decrease in the contact pairs, resulting in the resistance increase.

Figure 1c shows the fabrication procedure of 3DCS-based composite film, which consists of five steps. First, CNTs mixed with isopropyl alcohol (IPA) was coated on the donor substrate using spray coating (Figure 1c-i)). TEMs mixed with IPA was also uniformly coated on the substrate using spray coating (Figure 1c-ii)). As a result, the CNTs/TEMs layer was densely coated on the substrate (Figure S1, Supporting Information). Then, soft elastomer precursor was poured on the donor substrate that was already coated with CNTs/TEMs (Figure 1c-iii). After curing the elastomer, the composite film was peeled off from the donor substrate (Figure 1c-iv). Without TEMs expansion, the 2DCS-based composite film exhibits a smooth surface and the CNTs are densely embedded into the soft elastomer matrix forming a number of contact pairs as a flat 2D structure (Figure 1c-v). When the heat was applied to the composite films, the local CNTs structure changed from flat 2D to curved 3D due to large local strain caused by TEMs expansion (Figure 1c-vi). The photo of the fabricated 3DCS-based composite film is displayed in Figure 1d. Using spray coating method and elastomer casting, 3DCS-based composite film was successfully manufactured on the desired area. In addition, the CNT/TEMs layer was fully embedded inside the soft elastomer, and as a result, the 3DCS-based composite film exhibited high mechanical robustness under twisting, stretching, and bending deformation (Figure 1e). The current–voltage (I–V) characteristics of the composite films were measured to verify the resistance variation for changed CNTs percolation, as shown in Figure 1f. The linear I–V characteristics indicate good ohmic contacts or enough tunneling current between the CNTs. As the local CNT structure changed from flat 2D to curved 3D, the slope of I–V curve decreased due to the reduced conductive pathway between CNTs.

2.2. Characterization of Fabricated 3DCS

Figure 2a shows top and cross-sectional field emission scanning electron microscopy (FE-SEM) images of the fabricated composite film surfaces. The 2DCS-based composite film exhibited many wrinkled structures on the surface. When TEMs were expanded by heating, microdome structures were randomly generated across the entire substrate. The CNT networks could be also observed on the microdome structures. The profiles of 3DCS-based composite film were measured using a 3D confocal scanning microscope to observe the surface morphology. The irregular microdome structures with a maximum height of up to 80 μm were observed (Figure 2b). We checked the average height and uniformity of the 3DCS-based composite film by the comparing size distribution of microdome structures i) between three regions in a single sample and ii) between three different samples (Figure S2, Supporting Information). The average and standard

© 2023 Wiley-VCH GmbH

16136829, 2024, 2, Downloaded from https://onlinelibrary.wiley.com/doi/10.1002/smll.202303981 by Korea Advanced Institute Of, Wiley Online Library on [14/01/2024]. See the Terms and Conditions (https://onlinelibrary.wiley.com/terms-and-conditions) on Wiley Online Library for rules of use; OA articles are governed by the applicable Creative Commons License

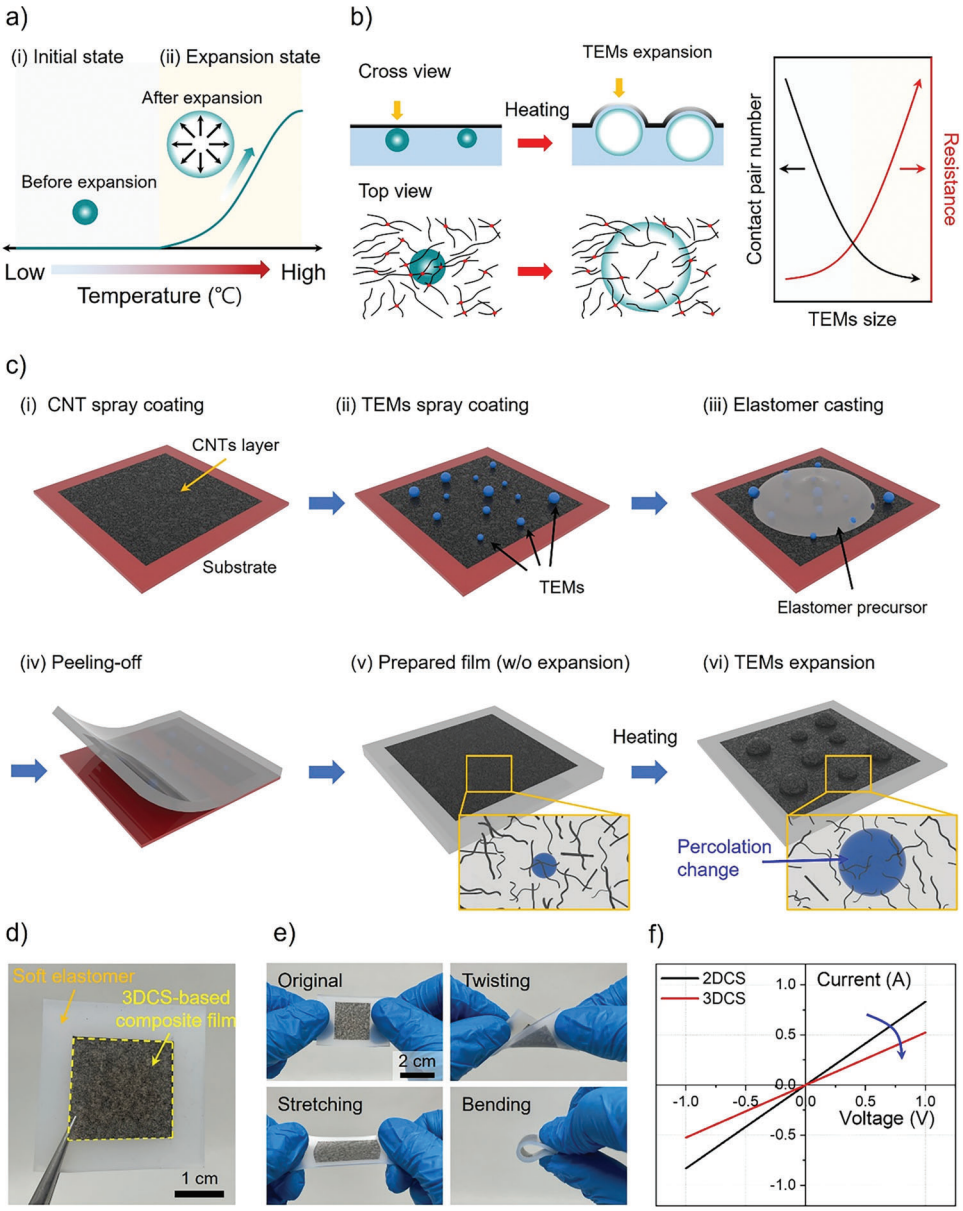


Figure 1. Concept and fabrication process of composite film with the local changes in curved 3D carbon nanotube (CNT) structure (3DCS). a) Expansion mechanism of thermally expandable microsphere (TEM). b) Schematic of the local changes in 3DCS using TEMs expansion. c) Fabrication process based on spray coating and thermal expansion of TEMs. d) Fabricated 3DCS-based composite films. e) Photographs indicating mechanical robustness under twisting, stretching, and bending deformation. f) The current–voltage (*I*–*V*) characteristics of the 2DCS and 3DCS-based composite films.

deviation of the microdome structures' sizes in the entire samples were measured as 64.8 ± 8.4 μm. In addition, measurement results showed similar tendencies with negligible deviations between different samples, indicating that the 3DCS-based composite film has excellent uniformity and reproducibility. Figure 2c shows the cross-sectional profiles along specific lines (AA′). In the case of AA′ (the horizontal direction), a dome structure with a maximum height of ≈65 μm was clearly observed along the 3D surface. The microdome structure of 3DCS-based composite film exhibited a rough surface due to the CNTs network inside the elastomer. In contrast, the microdome structure without CNTs coating showed a relatively smooth surface (Figure S3, Supporting Information). We also checked the 3D surface morphology (e.g., surface profiles, arithmetic mean height, and maximum height) of the 3DCS-based composite films with different TEMs concentrations (1, 3, and 5 wt%). The overall size increased by the aggregation of the TEMs, and much larger microdome structure with a maximum height of ≈320 μm was observed (Figure S4, Supporting Information).

To demonstrate the local change in curved 3D CNT structure using TEMs' expansion, real-time observation system was prepared. In this experiment, the optical transmittance of the composite film was changed by TEMs expansion, which was activated by a transparent polyimide (PI) heater (Figure 2d and Figure S5,

© 2023 Wiley-VCH GmbH

16136829, 2024, 2, Downloaded from https://onlinelibrary.wiley.com/doi/10.1002/smll.202303981 by Korea Advanced Institute Of, Wiley Online Library on [14/01/2024]. See the Terms and Conditions (https://onlinelibrary.wiley.com/terms-and-conditions) on Wiley Online Library for rules of use; OA articles are governed by the applicable Creative Commons License

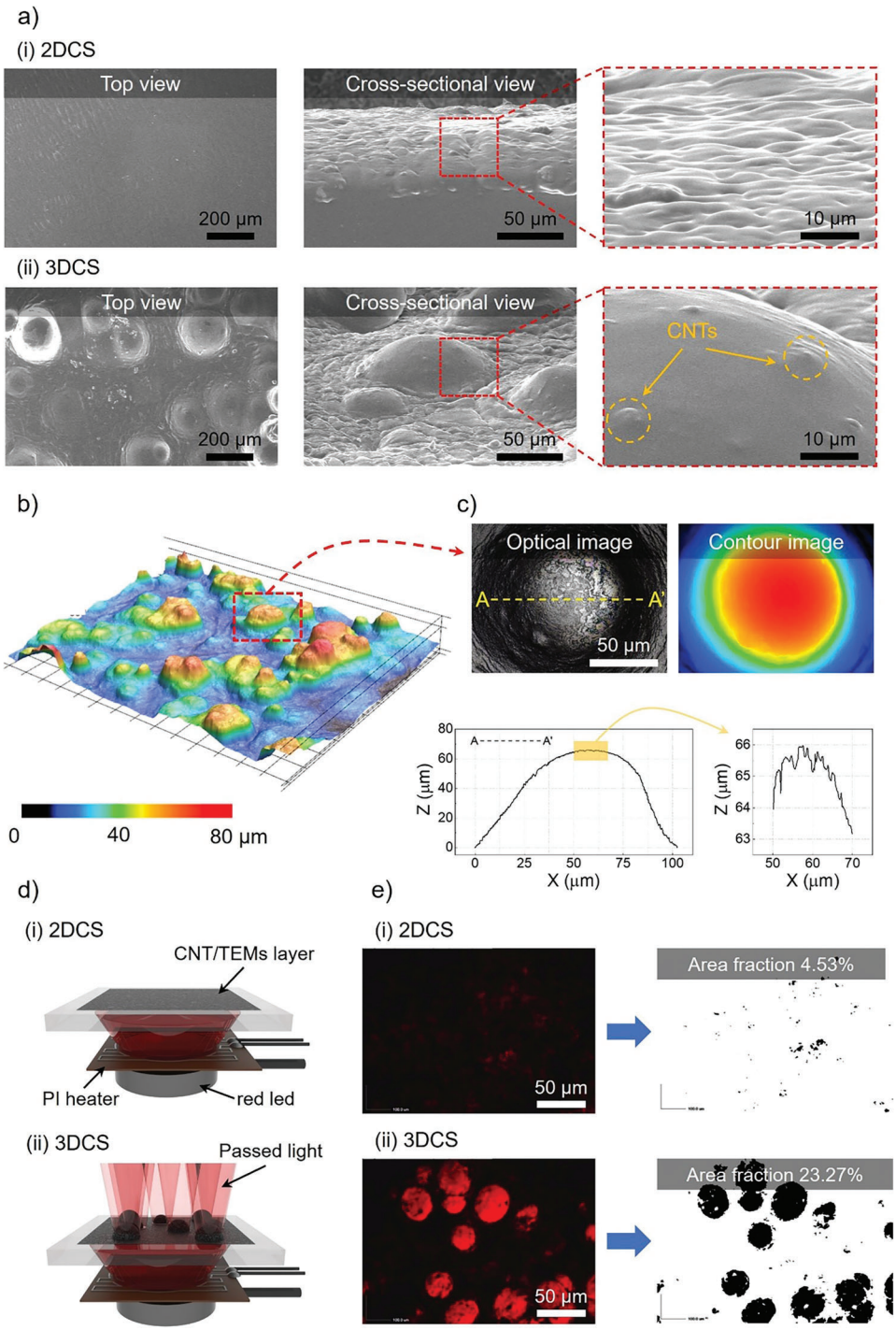


Figure 2. Field emission scanning electron microscopy (FE-SEM) images and surface observation of the flat 2DCS and curved 3DCS-based composite films. a) Top and cross-sectional FE-SEM images of composite films. With expansion of TEMs, microdome structures are generated thorough surface. b) Surface profile measurements of the 3DCS-based composite film. c) Cross-sectional profiles along specific lines (AA′) to observe the surface. A rough surface of about 1 μm was observed due to the CNT network inside the elastomer. d) Schematic illustration of composite film surface for verifying local change in 3D CNTs structure using transparent polyimide heater and red led. e) Observed and calculated area fraction of the flat 2DCS and curved 3DCS-based composite films. In case of 2DCS-based composite film, red-light cannot be transmitted owing to the high density of CNTs. In contrast, the 3DCS-based composite film passed a large amount of red-light by the 3D CNT percolation.

© 2023 Wiley-VCH GmbH

16136829, 2024, 2, Downloaded from https://onlinelibrary.wiley.com/doi/10.1002/smll.202303981 by Korea Advanced Institute Of, Wiley Online Library on [14/01/2024]. See the Terms and Conditions (https://onlinelibrary.wiley.com/terms-and-conditions) on Wiley Online Library for rules of use; OA articles are governed by the applicable Creative Commons License

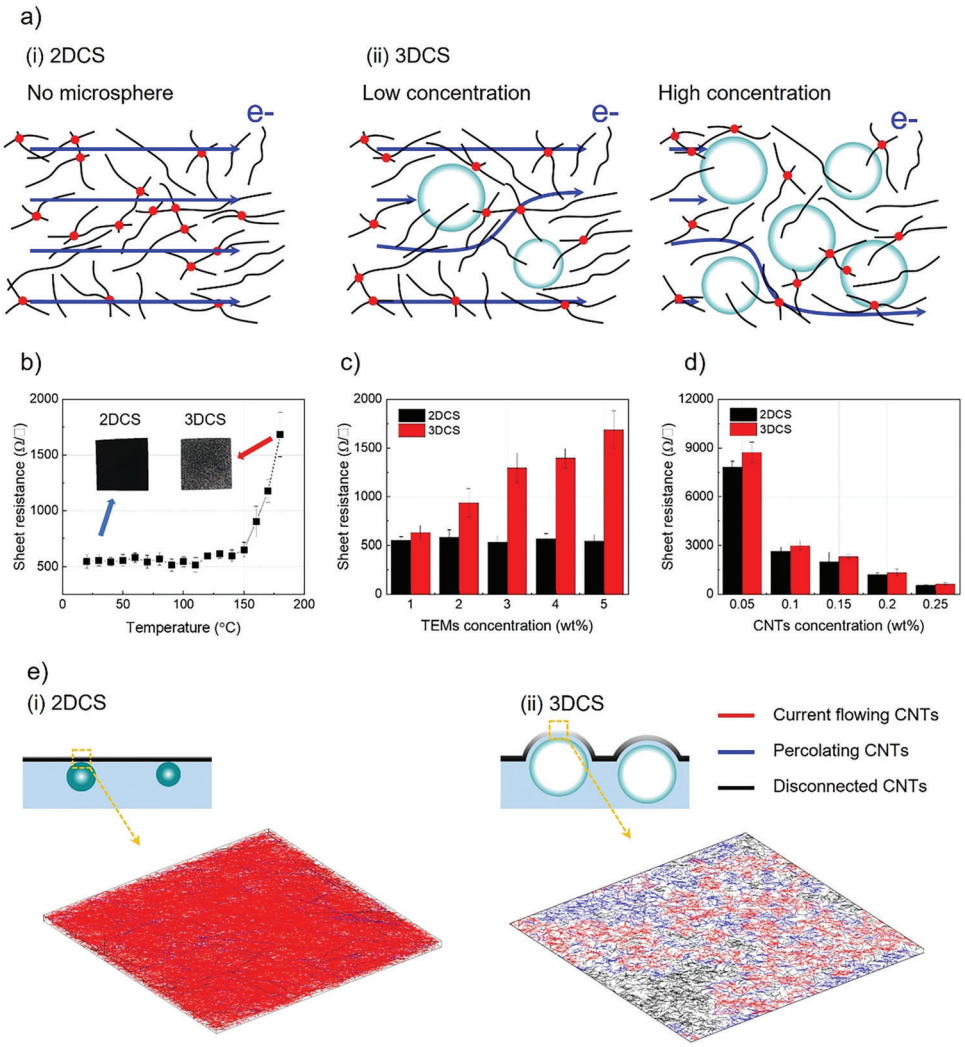


Figure 3. Electrical conductivity of the curved 3DCS-based composite films. a) Conductivity change mechanism of the composite films by changing local CNTs structure with TEM expansion and concentration. b–d) Measured sheet resistance of composite films according to temperature, TEM concentration, and CNT concentration. e) Numerical simulation to understand the local changes in CNTs percolation.

Supporting Information). In case of 2DCS-based composite film, red light was completely blocked owing to the high density of flat 2D CNT structure (Figure 2e-i). When the heat was applied to the composite film using a PI heater, the local CNT structure changed to curved 3D structures and the transmitted red light dramatically increased due to the loosening of the CNT network (Figure 2e-ii; Figure S6 and Video S1, Supporting Information). The area fraction of transmitted red light, which was calculated using optical images and threshold function of the Image J software, increased from 4.53% to 23.27%. These results mean that TEMs expansion changes local CNT percolation. In addition, fluorescent microspheres were combined with CNTs to visualize the alteration in CNTs network in response to the expansion of the TEMs. As illustrated in Figure S7, Supporting Information, CNTs-coated fluorescent microspheres were distinctly visible on top of the microdome structures, indicating that the CNTs remained present on the surface despite the high local strain caused by the microsphere expansion.

The CNT layer changes from a flat 2D to curved 3D structure by the TEMs expansion, leading to a decrease of the CNTs contact pairs and decreased electrical conductivity as a consequence. **Figure 3**a depicts mechanism of electrical conductivity by changing local CNTs percolation with TEMs' expansion and effect of TEMs' concentration. The conductivity of the composite film is determined by the CNT percolation embedded in the soft elastomer matrix. In the case of 2DCS-based composite film, a sufficient conductive pathway is formed due to the percolated CNTs inside the soft elastomer matrix. After TEMs' expansion, the flat 2D CNT layer is changed to a curved 3D structure, resulting in a decrease in the conductive pathway. In higher concentrations of TEMs, the electrical conductivity of the composite film is dramatically decreased due to the reduced contact pairs between CNTs. Therefore, the local CNT percolation and electrical conductivity of the composite film can be controlled via TEMs' expansion, which is also dependent on their concentrations. This could be confirmed by measuring the sheet

© 2023 Wiley-VCH GmbH

16136829, 2024, 2, Downloaded from https://onlinelibrary.wiley.com/doi/10.1002/smll.202303981 by Korea Advanced Institute Of, Wiley Online Library on [14/01/2024]. See the Terms and Conditions (https://onlinelibrary.wiley.com/terms-and-conditions) on Wiley Online Library for rules of use; OA articles are governed by the applicable Creative Commons License

resistance of the composite films under various conditions (e.g., applied temperature, concentration of TEMs, and CNTs). Figure 3b shows the measurement results for the composite film (TEMs 5 wt%, CNTs 0.05 wt%) by applying different heating temperatures. The initial sheet resistance was measured as 557.1 ± 37.3 Ω/□ at room temperature and showed a similar value up to 140 °C. At 150 °C, the sheet resistance started to increase as 653.2 ± 66.9 Ω/□, and continued to rise with the applied temperature (e.g., average sheet resistance of 1684.5 ± 199.4 Ω/□ at 180 °C). To demonstrate that the electrical conductivity of the composite films can be controlled according to TEMs' concentration, we fabricated the composite films with various TEMs concentrations of 1–5 wt% (CNTs 0.05 wt%) and measured the sheet resistance as shown in Figure 3c. The sheet resistance with TEMs' concentration of 1 wt% increased from 552.4 to 632.6 Ω/□ by TEMs' expansion. The sheet resistance change by TEMs' expansion significantly increased with the TEMs' concentration, eventually reaching 1684.5 Ω/□ at 5 wt% TEM concentration. In addition, the sheet resistance change of the composite films by the CNT concentration was evaluated (Figure 3d). Here, it should be noted that there was no significant difference in sheet resistance by the TEMs' expansion because the TEMs' concentration was as low as 1 wt%. As the CNT concentration increased from 0.05 to 0.25 wt%, the sheet resistance dramatically decreased from 7816.4 ± 382.6 to 781.2 ± 36.8 Ω/□. The trend of a sharp decrease as a function of the CNT concentration is consistent with the percolation theory, which predicts an exponential increase of the electrical conductivity in the vicinity of the percolation threshold.[21–23]

Numerical simulations were conducted using a percolation model to understand the local changes in curved 3D CNTs structure according to the TEMs expansion (Figure 3e). First, a 3D unit cell network model was generated in the soft elastomer matrix using a randomly distributed thin CNTs layer. Second, based on the measurement results of the sheet resistance, we assumed that about 5000 CNTs with constant aspect ratio (length/diameter ratio) of 1000 were randomly assigned within the soft elastomer matrix with width of $L_x = 40$ μm, length of $L_y = 40$ μm, and thickness of $L_z = 1$ μm. Third, we assumed that the local strain was assumed to be 650% based on the measurement results of microdome structure by the TEMs expansion (Figure S2, Supporting Information). The resistance of the total network was calculated using Kirchhoff's current law and Ohm's law after generating a network resistor model by junction between contact pairs of CNTs in the network. The junctions between two CNTs can be classified as three types: i) current flowing CNTs with no contact resistance, ii) percolated CNTs within a specific cutoff distance, and iii) disconnected CNTs.[24] We conducted a numerical simulation on the top point of TEMs expansion where large local strain (650%) occurs. As the figure shows, in the case of 2DCS-based composite film, most of the CNTs are current flowing state due to the high density of flat 2D CNT structures. However, a completely changed percolation model is observed in the case of 3DCS-based composite. Current flowing CNTs decreased significantly, percolated CNTs increased, and even disconnected CNTs were observed in the model of 3DCS-based composite film. The numerical simulation results suggest that the electrical properties of the composite film are dramatically changed with local changes in CNT percolation. In addition, the electrical properties of the composite film can be modulated by the TEMs expansion.

2.3. Pressure Sensor Development and Their Response Characterization

Figure 4a depicts the sensor structure based on 3DCS-based composite films. A metal interdigitated electrode (IDE) is fabricated on the flexible PI film, and 3DCS structure on the soft elastomer is in direct contact with this IDE electrode. When external pressure is applied to this structure, the irregular microdome structures contact the counter electrode, resulting in a rapid decrease in resistance, as shown in Figure 4b. Figure 4c shows the response of the soft pressure sensor using 2DCS and 3DCS-based composite films. The outcome demonstrates that the microdome structure on the CNT film is brought about by the TEMs expansion, and this has a major impact on the pressure sensitivity. The soft pressure sensor's sensitivity for a 2DCS-based sensor is 0.28 kPa^{-1} in the 0–10 kPa pressure range, whereas for a 3DCS–based sensor, the sensitivity rises to 571.64 kPa^{-1} in the 0–3 kPa range, 253.39 kPa^{-1} in the 3–5 kPa, and to 119.78 kPa^{-1} in the 5–10 kPa range. Notably, the sensitivity of the first linear section (0–3 kPa) is ≈2041 times higher than that of the sensor with 2DCS. Especially, the soft pressure sensor showed high linearity as 0.992 in the pressure range of 0–3 kPa, 0.977 in the pressure range of 3–5 kPa, and 0.983 in the pressure range of 5–10 kPa (Figure S8, Supporting Information). In this range, the pressurized, relatively large size irregular dome structure increases the electrical path network of the CNTs, which alters the sensor response. Above 3 kPa, additional electrical contacts made possible by relatively small microdome structures produce the sensor response matching to the pressure. We compared the sensitivity of two types of composite films (2DCS and 3DCS) by measuring the current–voltage (I–V) characteristics under different pressures (Figure S9, Supporting Information). The curves of the sensor with 2DCS almost overlapped, indicating low sensitivity, while the curves of the sensor with 3DCS changed significantly due to high sensitivity. The soft pressure sensor also shows negligible hysteresis of 5.34% at the pressure of 10 kPa, as shown in Figure S10, Supporting Information. Figure 4d shows the effects of the CNTs concentration on the sensor performance. The result shows that the optimum amount of the CNTs concentration is 0.1 wt%. At CNT concentration lower than 0.1 wt%, sufficient percolation between CNTs was not formed for their low density. Thus, even if the pressure is applied, the electrical pathway does not change significantly. On the other hand, CNTs concentrations higher than 0.1 wt% form sufficient conductive pathways due to their high density. Therefore, CNT percolation does not change significantly with applied pressure, which has less impact on the sensitivity of the sensor. In addition, we checked the effects of the thickness of the composite film. The 3DCS-based soft pressure sensors with different thicknesses showed similar response against the applied pressure (Figure S11, Supporting Information). The reason why the sensor sensitivity exhibited a similar response according to the film thickness is due to the stress concentration in the 3D microstructure formed on the surface of the composite film. When pressure is applied to 3DCS-based composite films of different thicknesses, stresses are concentrated in the microstructure, which changes the sensor response. Since the 3D microstructure on the surface is similar in size and density regardless of the thickness of elastomer, they showed the similar sensor sensitivity. Therefore, 3DCS-

 © 2023 Wiley-VCH GmbH

16136829, 2024, 2, Downloaded from https://onlinelibrary.wiley.com/doi/10.1002/smll.202303981 by Korea Advanced Institute Of, Wiley Online Library on [14/01/2024]. See the Terms and Conditions (https://onlinelibrary.wiley.com/terms-and-conditions) on Wiley Online Library for rules of use; OA articles are governed by the applicable Creative Commons License

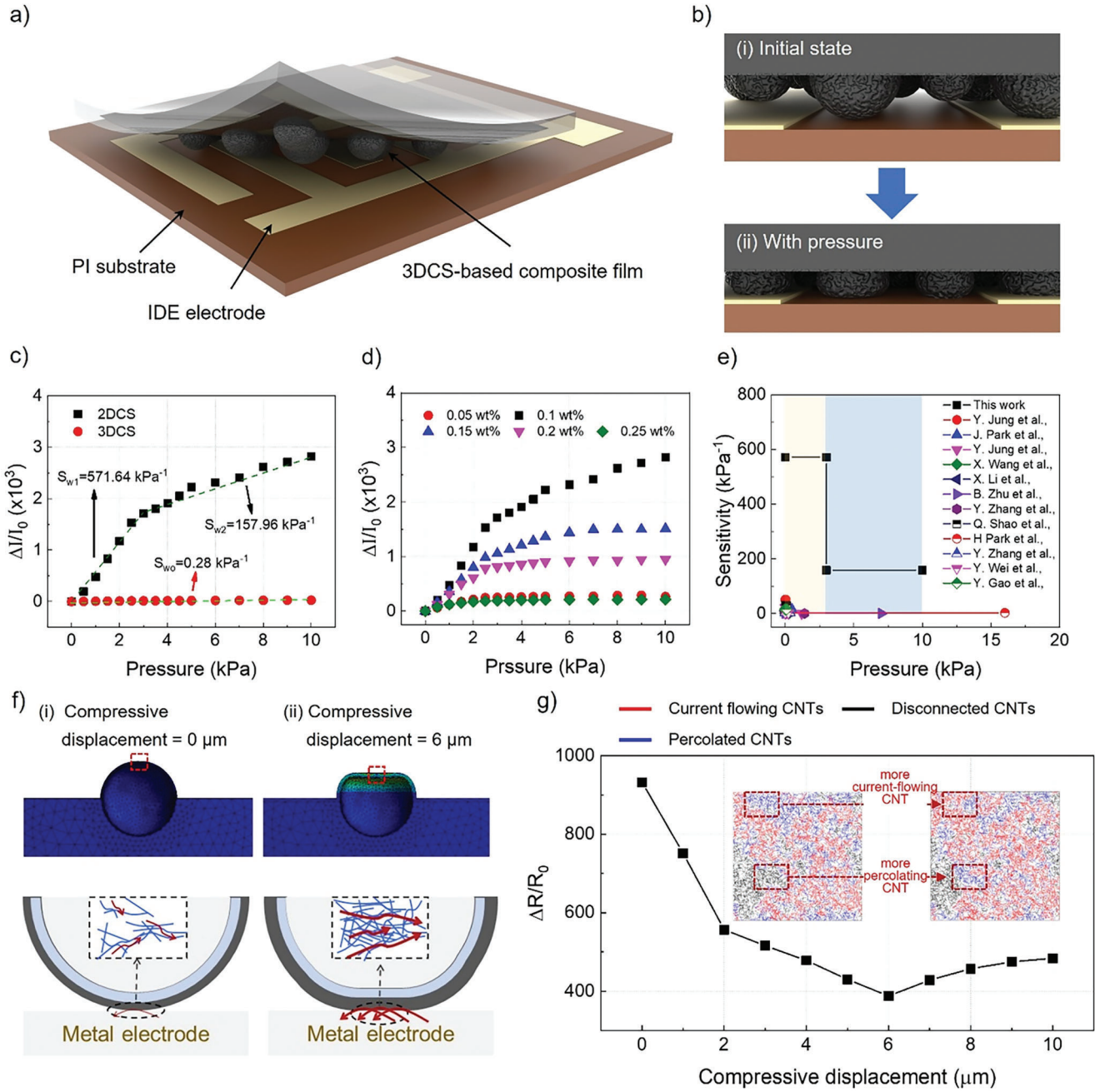


Figure 4. a) Schematic illustration of the soft pressure sensor with curved 3DCS. b) Sensing mechanism of the pressure sensor. c) Measured sensitivity of the soft pressure sensor under the pressure range 0–10 kPa. d) Pressure response characterization according to the amount of the CNT/IPA solution with applied pressure. e) Sensitivity comparison of the piezoresistive-type pressure sensor with previously developed microstructure-based pressure sensors. f) Schematic about the numerical simulation for verification of the high sensitivity of the sensor response which is induced by current change CNTs network at the top side of the microdome. g) Numerical simulation results depending on the compressive displacement of the microdome structure.

based composite film with the CNT concentration of 0.1 wt% and 2 mm thickness was used for the further characterization and wearable applications of the pressure sensor. Figure S12, Supporting Information, shows the sensor response for higher pressure range (10–50 kPa). Figure 4e and Figure S13, Supporting Information, compares the sensitivity of the proposed pressure sensor with those of other piezo-resistive and microstructure-based pressure sensors reported in the literature. As shown in this figure, our sensor has the highest sensitivity in low-pressure range among the microstructure-based piezoresistive pressure sensors. Figure S14, Supporting Information, demonstrates that five distinct pressure sensors produce consistent and comparable results in the pressure range of 0–10 kPa, exhibiting high reproducibility.

© 2023 Wiley-VCH GmbH

16136829, 2024, 2, Downloaded from https://onlinelibrary.wiley.com/doi/10.1002/smll.202303981 by Korea Advanced Institute Of, Wiley Online Library on [14/01/2024]. See the Terms and Conditions (https://onlinelibrary.wiley.com/terms-and-conditions) on Wiley Online Library for rules of use; OA articles are governed by the applicable Creative Commons License

Numerical simulation was conducted to understand the relationship between sensor's linear sensitivity and mechanical/electrical behavior of microdome structure under the applied pressure, as shown in Figure 4f. First, finite element simulations were performed to analyze the deformation mechanism of the microdome structure under various compressive displacement, as shown in Figure S15a, Supporting Information. The TEMs are embedded in the elastomeric matrix and covered by an elastomer shell. To observe the surface deformation, a single microdome structure was subjected to compressive displacement ranging from 0 to 10 μm. This behavior is depicted in Figure S15b, Supporting Information. Second, the percolation network analysis model for CNT/elastomer nanocomposite was utilized to observe the change of CNT percolation network and current flowing through the network when the pressure is applied. Figure S16a, Supporting Information, illustrates the various locations on a sphere based on their angles relative to the center of the sphere, namely 90°, 60°, 45°, and 30°. By combination of these two different simulations, the resistance change of CNT network from the initial state to 10 μm displacement could be calculated at the top side ($\theta = 90°$) of the microdome, as shown in Figure 4g. At the initial state, there are fewer interconnected CNTs caused by the TEMs' expansion, However, when a compressive displacement of 6 μm is applied, more interconnected CNTs are generated, resulting in lower resistance of CNT network (Figure 4g). The numerical simulation results show that compression occurs at the top of the microdome structure, increasing the CNT percolation, which greatly reduces the resistance of the top of the microdome. These results indicate that the sensitivity of the developed soft pressure sensor is dramatically enhanced by the synergistic effect of i) the heterogeneous contact change in irregular microdome structures and ii) the contact pair increase within the curved 3D CNTs structure under the applied pressure.

We studied a soft pressure sensor in various ways to understand its capabilities. We also measured the repeatability of the sensor's response to pressure and found that it provided reliable and stable signals over different pressure ranges, as shown in **Figure 5**a. We observed the sensor's response to dynamic pressure loading at different speeds and found that it was negligibly affected by speeds from 2 to 10 mm s^{-1} (Figure 5b). Additionally, we evaluated the dynamic response characteristics of the sensor and measured the rising and falling times (Figure 5c). The measured 10 to 90% rising time (t_r) was 47 ms, and the 90 to 10% falling time (t_d) was 85 ms. We tested the sensor's long-term stability by applying 5000 cycles of 10 kPa pressure and found that the values slightly increased after 5000 cycles (Figure 5d). In the first ten cycles, the average response was 2848 with a standard deviation of 2.21%. In cycles 4991–5000, the average response and standard deviations were 3113% and 1.34%, respectively. Despite being compressed many times, the values slightly increased after 5000 cycles. Additionally, we observed the surface profile of the 3DCS-based composite film before and after the cyclic test and found no significant structural deformation (Figure S17, Supporting Information). A 10 min holding period was employed following the application of pressure, and the corresponding changes in current were monitored at 1, 5, and 10 kPa (Figure S18, Supporting Information). Relative to the initial response upon pressure application, the final response after the 10 min holding period exhibited a decrease of 25%, 22%, and 18% for pressures of 1, 5, and 10 kPa, respectively. This continuous decline in resistance can be attributed to the interaction between the microdome and elastomer within the material upon the application of pressure. Furthermore, by defining the time required for the sensor's current flow to stabilize as the duration to reach 90% of the value held for 600 s, stabilization times of 80, 40, and 16 s were observed at 1, 5, and 10 kPa, respectively.

2.4. Demonstration of the Pressure Sensor on the Wearable System and Pressure Array Pad

The soft pressure sensor with 3DCS-based composite film has excellent sensing performance and fabrication flexibility, making it suitable for various practical applications. To demonstrate its potential applications, we tested the sensor as i) a wearable healthcare sensor to monitor wrist pressure during daily mouse use to prevent carpal tunnel syndrome (CTS) and ii) a multi-array pressure sensor to detect spatial pressure and movements. Daily activities, including computer and tablet use, can lead to CTS, and extended mouse usage time can put pressure on the carpal tunnel. To prevent CTS, we developed a wristband structure with four pressure monitoring sensors integrated into the designated location of the wrist, as shown in **Figure 6**a. The data was transmitted via Bluetooth to a smartphone app for real-time monitoring. When the pressure reaches a specific level, a warning signal is triggered. Figure 6b shows the sensor monitoring three different gripping paradigms (e.g., palm grip and claw grip in normal mouse, vertical mouse) during this demonstration.

We conducted several independent experiments to compare the effects of different actions on the pressure applied to the wrist during mouse usage. Seven different actions were tested, including clicking the mouse, bending the wrist to the left and right, moving the mouse forward, backward, right, and left. As shown in Figure 6c–e, the results showed that using a normal mouse generally puts more pressure on the wrist than using a vertical mouse, which can cause wrist strain (Videos S2 and S3, Supporting Information). The S_{bl} sensor (located at the bottom/left position of the wrist) was highly affected by the wrist bending motion. In addition, the S_{ur} sensor (located at the upper/right position of the wrist) was found to experience relatively high pressure (≈20 kPa) during the claw grip motion with the normal mouse, which can damage the wrist with long-term usage. However, the vertical mouse was effective in reducing the pressure on the CT site and preventing such strain. Furthermore, the developed system was utilized to measure the repeated signal from the wrist bending motion, as demonstrated in Figure S19, Supporting Information. The results exhibit consistent and repeatable measurements across the entire system. Additionally, the signal-to-noise ratio (SNR) of the device itself can be calculated based on the equation below.

$$\mathrm{SNR}_{\mathrm{dB}} = \log\left(\frac{\mu^2}{\sigma^2}\right) \quad (1)$$

where μ is the average value of the signal and σ is the noise when there is no input signal. The calculated SNR based on

© 2023 Wiley-VCH GmbH

16136829, 2024, 2, Downloaded from https://onlinelibrary.wiley.com/doi/10.1002/smll.202303981 by Korea Advanced Institute Of, Wiley Online Library on [14/01/2024]. See the Terms and Conditions (https://onlinelibrary.wiley.com/terms-and-conditions) on Wiley Online Library for rules of use; OA articles are governed by the applicable Creative Commons License

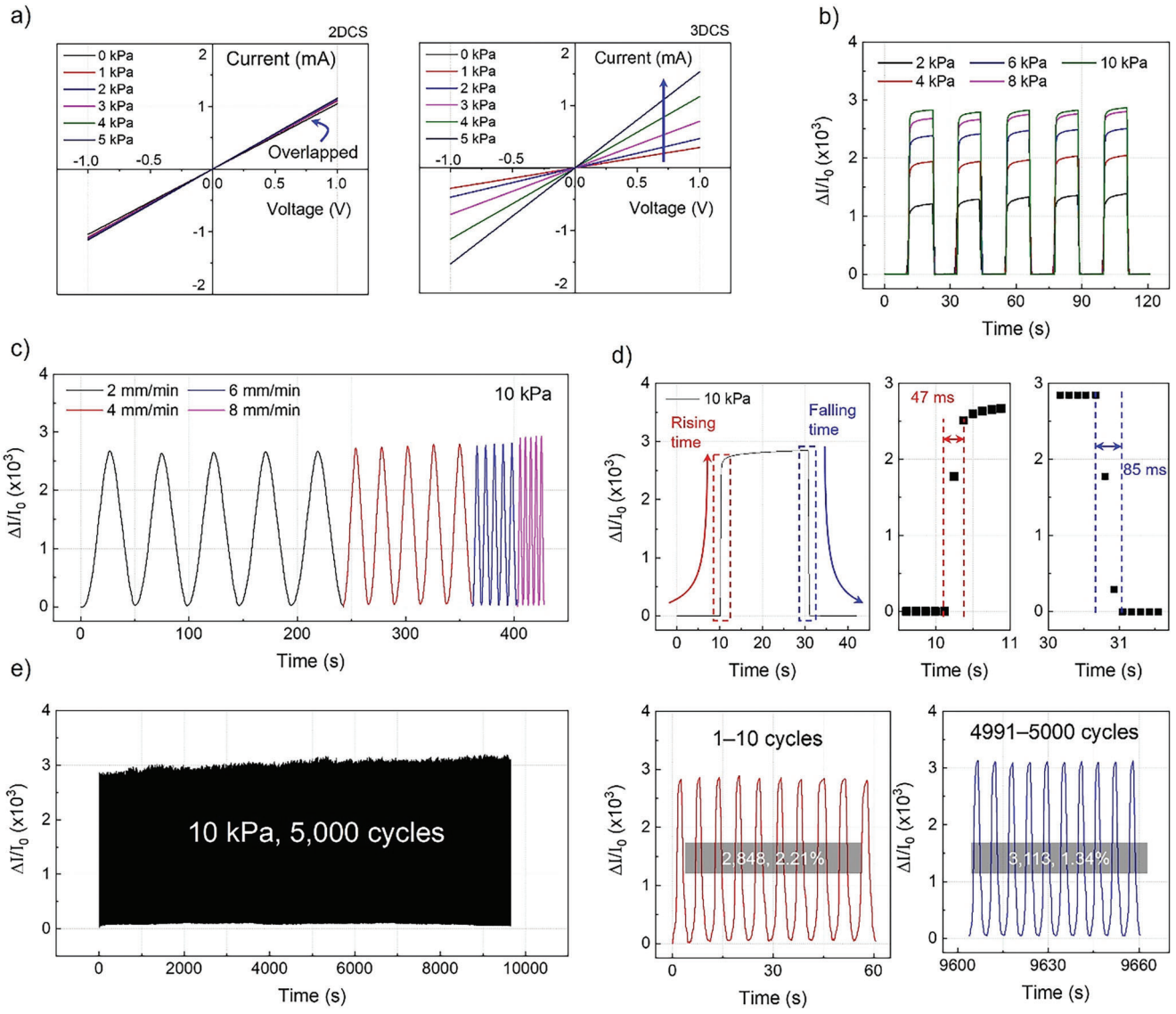


Figure 5. Analysis of the sensor performance under static and dynamic loading conditions. b) Repeatability test of the pressure sensor under various applied pressures (2, 4, 6, 8, and 10 kPa). c) Dynamic response of the pressure sensor under various pressure speed ranges (2, 4, 6, and 8 mm s^{-1}) with pressure range 0–10 kPa. d) Response time of the soft pressure sensor for a compressive loading of 10 kPa. e) Reliability test by cyclic loading of 10 kPa over 5000 cycles. The red and blue graphs show the result of each ten cycles for the initial (1–10 cycles) and the last (4991–5000 cycles).

the signal delivered from the Arduino is as high as 4.7. These ergonomic tools were found to be effective in reducing pressure on the wrist during mouse activity, as demonstrated in the experiment.

In another demonstration of practical applications of the proposed technology, a multi-array pressure sensor was developed (**Figure 7**). Our proposed soft pressure sensor is easily scalable, making it ideal for large-scale pressure sensor arrays. It exhibits excellent sensing performance in the low-pressure range, making it capable of detecting subtle pressure such as soft touch. By connecting the sensor pad to a computer, we can create a mapping system that displays the location and intensity of pressure applied to the pad. Figure 7a,b shows the design of a multi-array pressure sensor consisting of two parts: the top active layer and the bottom counter electrode. The multi-array pressure sensor with 10 × 16 pixels was fabricated using masking, metal-deposition, and screen-printing processes. A detailed description of the multi-array pressure sensor fabrication is presented in the Experimental Section. Figure 7c shows an image of the fabricated multi-array pressure sensor with a total size of 60 × 80 mm^2. A flexible printed circuit board and software were used to measure the pressure on each pixel when pressure was applied to the sensor array pad. In Figure 7d, we can see the results of measuring the spatial pressure of Korean chess pieces of different sizes and weights (ranging from 4.3 to 10.1 g). To improve the resolution and provide a visual representation, a 2D mapping and interpolation approach was applied to the sensor signals. This allowed for accurate prediction of

© 2023 Wiley-VCH GmbH

16136829, 2024, 2, Downloaded from https://onlinelibrary.wiley.com/doi/10.1002/smll.202303981 by Korea Advanced Institute Of, Wiley Online Library on [14/01/2024]. See the Terms and Conditions (https://onlinelibrary.wiley.com/terms-and-conditions) on Wiley Online Library for rules of use; OA articles are governed by the applicable Creative Commons License

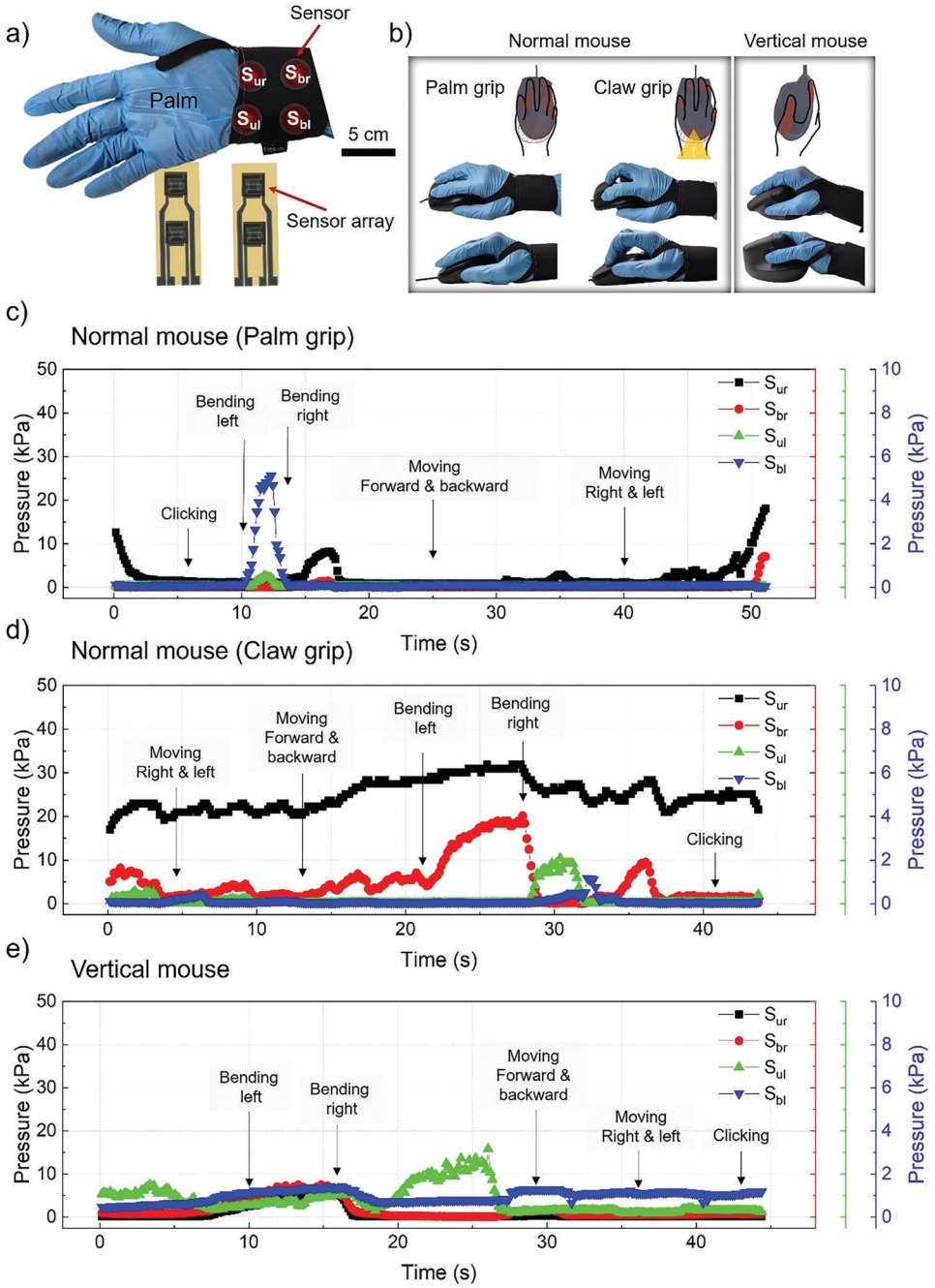


Figure 6. Application to the smart wristband to prevent carpal tunnel syndrome (CTS) during mouse use. a) Schematic of the sensor position on the wristband. b) Three different postures of the mouse grip. Responses from the soft pressure sensors during sequential operation of clicking the mouse, bending the wrist to the left and right, moving the mouse forward, backward, right, and left with c) the normal mouse palm grip, d) normal mouse claw grip, and e) vertical mouse.

pressure levels at nearby locations with a limited number of sensing points. In addition, the multi-array pressure sensor was used for dynamic detection, such as drawing movement (as shown in Figure 7e). A pencil was used to draw a circular curve on the sensor, and each pixel in the sensor showed a change in resistance value. The pressure sensor was able to successfully detect the pressure level and location of the touch input in real-time.

3. Conclusion

This study presented a new method for fabricating highly sensitive soft pressure sensors using microstructures based on curved 3D CNT structures. The technique involves the expansion of TEMs to alter the contact pairs in the CNT network and increase the contact area between the active layer and IDE. This improves the sensor's sensitivity, which was found to be 571.64 kPa^{-1} in

© 2023 Wiley-VCH GmbH

16136829, 2024, 2, Downloaded from https://onlinelibrary.wiley.com/doi/10.1002/smll.202303981 by Korea Advanced Institute Of, Wiley Online Library on [14/01/2024]. See the Terms and Conditions (https://onlinelibrary.wiley.com/terms-and-conditions) on Wiley Online Library for rules of use; OA articles are governed by the applicable Creative Commons License

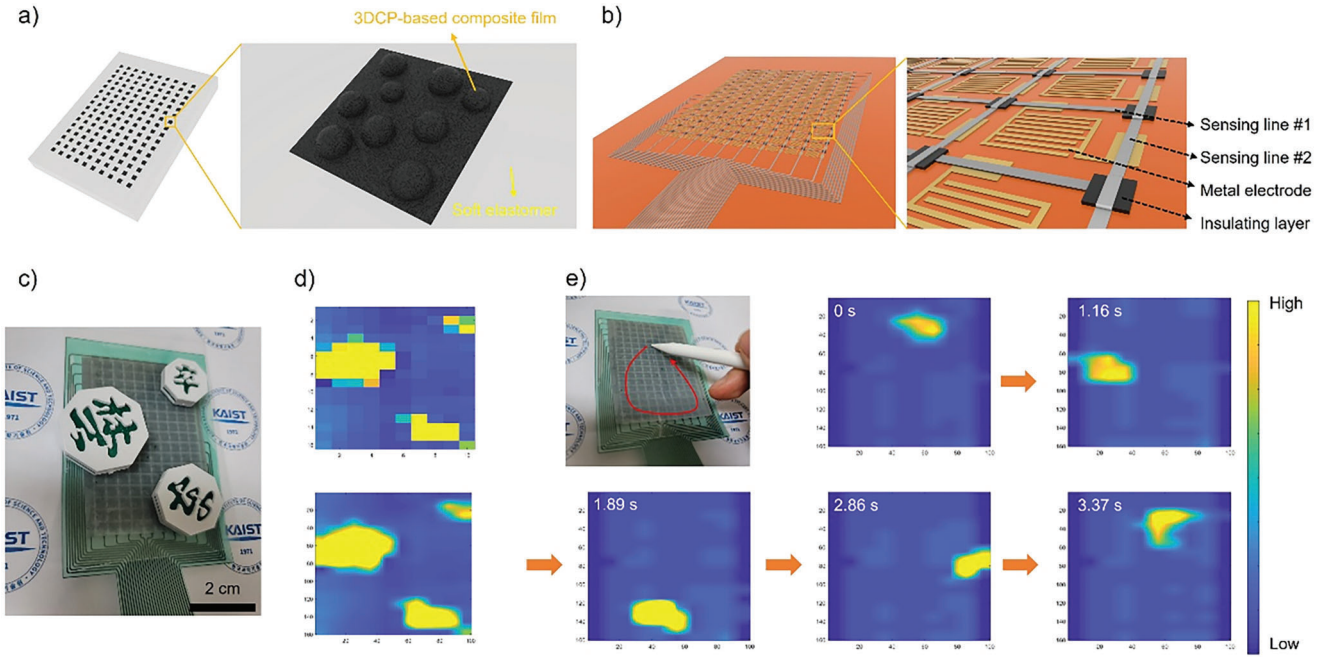


Figure 7. Demonstration of the multi-array pressure sensor with 10 × 16 pixels for realizing a variety of movements in real-time. a,b) Schematic illustration of the top active layer and bottom counter electrode. c) Images of the fabricated multi-array pressure sensor to detect and distinguish spatial pressure of Korean chess pieces with different weights and sizes. d) The corresponding response results of the multi-array pressure sensor using 2D mapping and interpolation technique. e) Real-time measurement for the dynamic movement of the pencil on multi-array pressure sensor.

the low-pressure range, higher than other studies. The sensor has excellent repeatability, a fast response time of 85 ms, and long-term stability. The relationships between sensor sensitivity and mechanical/electrical behavior of the microdome structure have been successfully demonstrated using the finite-element method simulation. The sensor was used in a wireless wearable health monitoring system to prevent CTS and a multi-array pressure sensing system. As a result of our experiments, we have found that using the 3D surface shape of TEMs to vary the CNT percolation can create low-range pressure sensors with high sensitivity, flexibility, scalability, and reliability. This study introduced a new approach to designing pressure sensors with excellent sensing performance in the low-pressure range using 3D surface geometry. These findings will pave the way for developing highly advanced pressure sensors for various applications, such as health monitoring systems and human–machine interfaces.

4. Experimental Section

Fabrication of the Curved 3DCS-Based Composite Film: First, multi-wall CNTs (MR99, Carbon Nano-material Technology Co., Ltd., Republic of Korea) were mixed with IPA and sprayed on a PI substrate. The coating density was controlled by the amount of the solution used. Thermally expandable microspheres (MSH-550, SDI Korea, Republic of Korea) were also mixed with IPA and spray-coated onto the substrate where the CNT was coated. The dragon skin prepolymer (Dragon Skin 30, Smooth-On, Inc., USA) was prepared by mixing it with a curing agent at a weight ratio of 1:1. The mixed prepolymer was poured onto the substrate where CNT and TEM were coated, and then cured at 60 °C for 2 h. The fully cured 2DCS-based composite film was peeled off. The 2DCS-based composite film was then heated at 180 °C for 5 min to expand the TEMs to their optimal size.

Characterization of the Curved 3DCS Composite Film: A FE-SEM film (FE-SEM, Sirion, Thermo Fisher Scientific, Inc., Waltham, MA, USA) was used to observe the morphologies of the film, while a 3D laser scanning confocal microscope (VX-X1050, KEYENCE, Japan) was used to examine the 3D surface. Real-time images were obtained of the 2DCS and 3DCS-based area fraction calculation images using an optical microscope (AM7013MZT4, Dino-Lite Digital Microscope, Republic of Korea), and fluorescent microspheres were also observed using a fluorescent microscope (AM4115T-GRFBGY, Dino-Lite Digital Microscope, Republic of Korea). The sheet resistance of the composite films was measured with a four-point probe (CMT-SR2000N, Advanced Instrument Technology, Korea), and the average and deviation were calculated by measuring ten points for each condition. A high-precision universal testing machine (AGS-X [1 kN], Shimadzu Corporation, Japan) equipped with a load cell (maximum load = 1000 N) was utilized to test the sensing capability. The sensor response was measured using a source meter (2400, Keithley, USA).

Simulation of Compressive Behavior of the Microdome Structure: To better understand the behavior of the microdome structure, finite element simulations were performed using ANSYS software. A model was created with a microdome that had a radius of 32.5 µm and a wall thickness of 1 µm, embedded near the top surface of a polymer layer that was 1 µm thick. The simulation was performed on half of the geometry based on its symmetry, and consisted of 51735 nodes and 26730 elements. Deformation was simulated by applying displacements of up to 10 µm in the compressive direction on the top surface of the microdome. The elastic modulus and Poisson's ratio of the microdome and substrate were assumed to be 90 kPa and 0.49, respectively.

Simulation of CNTs Network: It was assumed that CNTs were cylindrical rigid bodies that created percolation due to their high modulus and simplicity in mathematics. It was also assumed that the position and orientation of the CNTs were transformed based on the deformation of the

© 2023 Wiley-VCH GmbH

16136829, 2024, 2, Downloaded from https://onlinelibrary.wiley.com/doi/10.1002/smll.202303981 by Korea Advanced Institute Of, Wiley Online Library on [14/01/2024]. See the Terms and Conditions (https://onlinelibrary.wiley.com/terms-and-conditions) on Wiley Online Library for rules of use; OA articles are governed by the applicable Creative Commons License

matrix, and the periodic boundary condition was applied. The researchers analyzed the connectivity of CNTs by calculating their distances and determining whether they were in contact or not. This information was used to identify CNT networks using depth-first search algorithms. Finally, Kirchhoff's current law was used to calculate the theoretical conductivity of the percolated networks.

Fabrication of the Soft Pressure Sensor: In this study, an IDE was fabricated on a PI film that was placed on a silicon wafer. The PI film was spin-coated on the Si wafer, and then baked in an oven at 150 °C for 1 h and at 260 °C for 4 h. The IDE pattern was fabricated using a process called photolithography with AZ5214E photoresist on the PI film.[17] To deposit the electrode layer (Titanium [Ti] = 30 nm, for adhesion/gold [Au] = 50 nm for conductance) on the patterned PR, an electron-beam evaporator was used. After the IDE was fabricated, a 3DCS composite film was placed on top of it.

Fabrication of the Wearable System for Wrist Pressure Monitoring: The system used to monitor wrist pressure was created by following several steps. First, the conductive fiber tape was cut by a laser in a specific pattern and placed onto a polyethylene terephthalate (PET) film. Four different PET films with conductive patterns were made and covered with 3DCS-based composite film. The pressure sensors were then placed on the wrist and secured with medical tape (3M Micropore Tan Surgical Tape, 3M Inc., USA). The wireless system was made up of an Arduino (nano33 IoT device) device and a smartphone app developed using MIT App Inventor. This allowed a mobile phone equipped with Bluetooth 3.0 to receive signals sent by the Arduino device. This experiment was approved by the institutional review board (IRB) of Korea Advanced Institute of Science and Technology (IRB no. KH2023-001).

Fabrication of the Multi-Array Pressure Sensor: In this study, a multi-array pressure sensor was fabricated by following a set of steps. First, a patterned PI film was fabricated by laser cutting. The substrate was then sprayed with CNTs mixed with IPA and TEMs mixed with isopropyl alcohol. After removing the patterned PI film, the prepolymer elastomer was poured onto the substrate and cured at 60 °C for 2 h. A top active layer consisting of 10 × 16 pixels was manufactured after heat treatment at 180 °C for 5 min. A bottom counter electrode of 10 × 16 pixels was also fabricated using a metal-deposition and screen printing. A shadow mask with an IDE pattern was mounted on the PI substrate, and a metal layer (Ti = 10 nm, Au = 50 nm) was deposited by sputtering to fabricate the metal IDE pattern with 10 × 16 pixels.

Supporting Information

Supporting Information is available from the Wiley Online Library or from the author.

Acknowledgements

This research was supported by the National Research Foundation of Korea (NRF) grant funded by the Korea government (MSIT) (No. 2021R1A2C3008742), the Basic Science Research Program through the National Research Foundation of Korea (NRF) funded by the Ministry of Education (No. RS-2023-00246712), and Alchemist Project grant funded by Korea Evaluation Institute of Industrial Technology (KEIT) and the Korea Government (MOTIE) (Project Number: 1415179744, 20019169).

Conflict of Interest

The authors declare no conflict of interest.

Author Contributions

Y.J. and J.G. contributed equally to this work. The manuscript was written through contributions of all authors. All authors have given approval to the final version of the manuscript.

Data Availability Statement

Research data are not shared.

Keywords

carbon nanotube percolation, high sensitivity, microdome structures, soft pressure sensors, thermally expandable microspheres

Received: May 12, 2023
Revised: August 4, 2023
Published online: September 5, 2023

[1] X. Wang, L. Dong, H. Zhang, R. Yu, C. Pan, Z. L. Wang, *Adv. Sci.* **2015**, *2*, 1500169.
[2] W. Honda, S. Harada, T. Arie, S. Akita, K. Takei, *Adv. Funct. Mater.* **2014**, *24*, 3299.
[3] K. Kim, J. Choi, Y. Jeong, I. Cho, M. Kim, S. Kim, Y. Oh, I. Park, *Adv. Healthcare Mater.* **2019**, *8*, 1900978.
[4] M. Zhong, L. Zhang, X. Liu, Y. Zhou, M. Zhang, Y. Wang, L. Yang, D. Wei, *Chem. Eng. J.* **2021**, *412*, 128649.
[5] S. Chen, S. Peng, W. Sun, G. Gu, Q. Zhang, X. Guo, *Adv. Mater. Technol.* **2019**, *4*, 1800681.
[6] J. Park, Y. Lee, J. Hong, M. Ha, Y. Do Jung, H. Lim, S. Y. Kim, H. Ko, *ACS Nano.* **2014**, *8*, 4689.
[7] Y. Jung, K. K. Jung, D. H. Kim, D. H. Kwak, S. Ahn, J. S. Han, J. S. Ko, *Sens. Actuators, A.* **2021**, *331*, 113034.
[8] X. Wang, Y. Gu, Z. Xiong, Z. Cui, T. Zhang, *Adv. Mater.* **2014**, *26*, 1336.
[9] O. Atalay, A. Atalay, J. Gafford, C. Walsh, *Adv. Mater. Technol.* **2018**, *3*, 1700237.
[10] B. C. K. Tee, A. Chortos, R. R. Dunn, G. Schwartz, E. Eason, Z. Bao, *Adv. Funct. Mater.* **2014**, *24*, 5427.
[11] Y. Jung, T. Lee, J. Oh, B. G. Park, J. S. Ko, H. Kim, J. P. Yun, H. Cho, *ACS Appl. Mater. Interfaces.* **2021**, *13*, 28975.
[12] S. R. A. Ruth, Z. Bao, *ACS Appl. Mater. Interfaces.* **2020**, *12*, 58301.
[13] Y. Hu, C. Xu, Y. Zhang, L. Lin, R. L. Snyder, Z. L. Wang, *Adv. Mater.* **2011**, *23*, 4068.
[14] J. Choi, D. Kwon, B. Kim, K. Kang, J. Gu, J. Jo, K. Na, J. Ahn, D. Del Orbe, K. Kim, J. Park, J. Shim, J. Y. Lee, I. Park, *Nano Energy.* **2020**, *74*, 104749.
[15] Y. Jung, K. K. Jung, D. H. Kim, D. H. Kwak, J. S. Ko, *Polymers.* **2020**, *12*, 1499.
[16] Y. Jung, J. Choi, W. Lee, J. S. Ko, I. Park, H. Cho, *Adv. Funct. Mater.* **2022**, *32*, 2201147.
[17] Y. Jeong, J. Gu, J. Byun, J. Ahn, J. Byun, K. Kim, J. Park, J. Ko, J. ho Jeong, M. Amjadi, I. Park, *Adv. Healthcare Mater.* **2021**, *10*, 2001461.
[18] Y. Zhang, Y. Hu, P. Zhu, F. Han, Y. Zhu, R. Sun, C. P. Wong, *ACS Appl. Mater. Interfaces.* **2017**, *9*, 35968.
[19] S. Baek, H. Jang, S. Y. Kim, H. Jeong, S. Han, Y. Jang, D. H. Kim, H. S. Lee, *RSC Adv.* **2017**, *7*, 39420.
[20] T. Yang, W. Deng, X. Chu, X. Wang, Y. Hu, X. Fan, J. Song, Y. Gao, B. Zhang, G. Tian, D. Xiong, S. Zhong, L. Tang, Y. Hu, W. Yang, *ACS Nano.* **2021**, *15*, 11555.
[21] Y. Jung, J. Ahn, J. S. Kim, J. H. Ha, J. Shim, H. Cho, Y. S. Oh, Y. J. Yoon, Y. Nam, I. K. Oh, J. H. Jeong, I. Park, *Small Methods.* **2022**, *6*, 2200248.
[22] Y. D. Shi, J. Li, Y. J. Tan, Y. F. Chen, M. Wang, *Compos. Sci. Technol.* **2019**, *170*, 70.
[23] X. F. Sánchez-Romate, A. Jiménez-Suárez, M. Sánchez, A. Güemes, A. Ureña, *RSC Adv.* **2016**, *6*, 43418.
[24] M. Amjadi, A. Pichitpajongkit, S. Lee, S. Ryu, I. Park, *ACS Nano.* **2014**, *8*, 5154.

© 2023 Wiley-VCH GmbH

16136829, 2024, 2, Downloaded from https://onlinelibrary.wiley.com/doi/10.1002/smll.202303981 by Korea Advanced Institute Of, Wiley Online Library on [14/01/2024]. See the Terms and Conditions (https://onlinelibrary.wiley.com/terms-and-conditions) on Wiley Online Library for rules of use; OA articles are governed by the applicable Creative Commons License